第132巻　第 6 号　2024年 6 月 1 日発行（毎月1回1日発行）　ISSN 1348-6535 CODEN: JCSJEW

JCS-Japan

June

vol.132

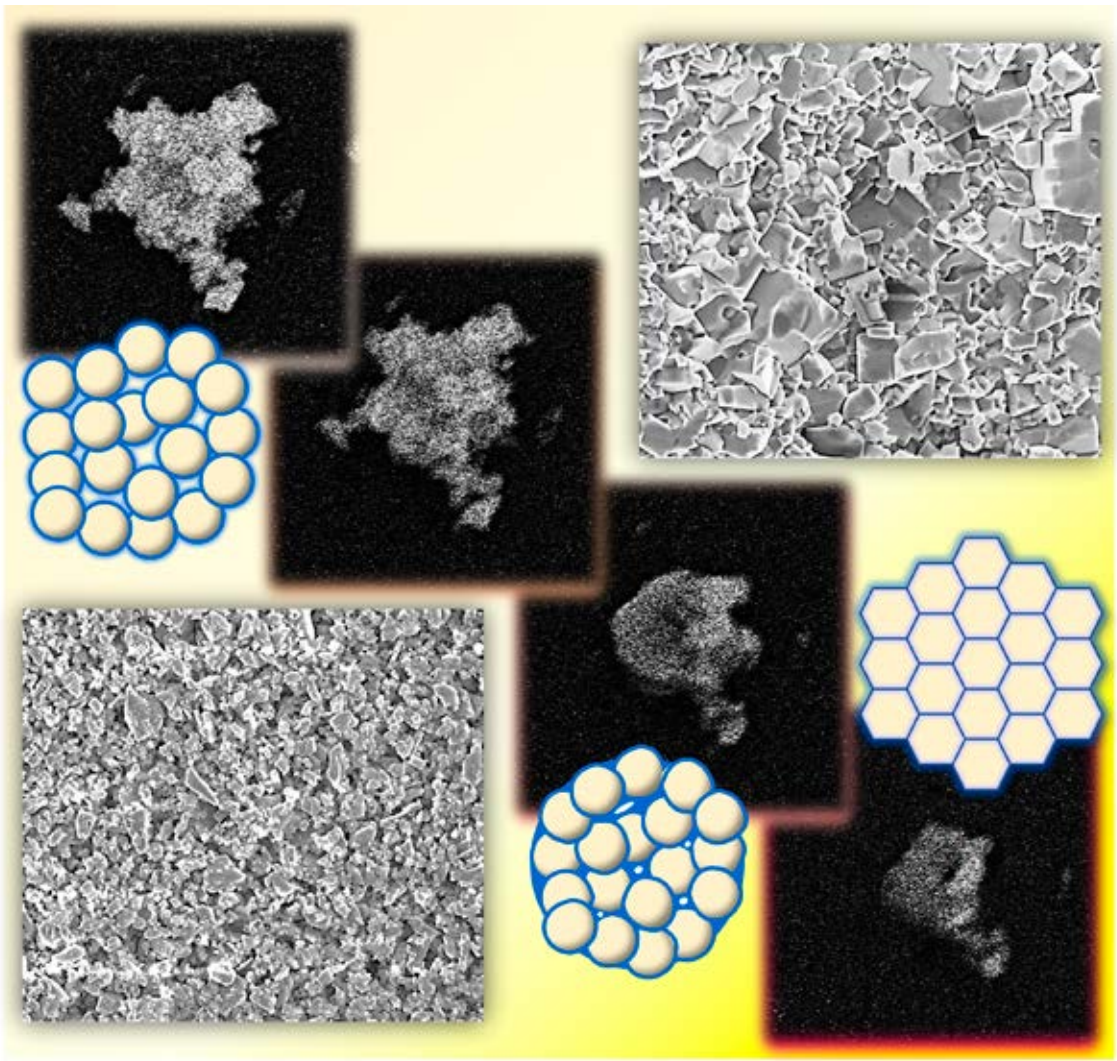

Journal of the Ceramic Society of Japan

2024

Journal of the Ceramic Society of Japan 132 [6] 257-266 2024
DOI https://doi.org/10.2109/jcersj2.23208

JCS-Japan

FULL PAPER

Surface modification of Li_3PO_4 to $Li_{1.3}Al_{0.3}Ti_{1.7}(PO_4)_3$ by wet chemical process and its sintering behavior

Kento Ishii[1,†], Yuri Taniguchi[2], Akira Miura[3], Shogo Miyoshi[4], Kazunori Takada[4], Go Kawamura[2], Hiroyuki Muto[2], Atsunori Matsuda[2], Masayoshi Fuji[1] and Tetsuo Uchikoshi[4,‡]

[1]Nagoya Institute of Technology, Advanced Ceramics Research Center, 3–101–1 Honmachi, Tajimi, Gifu 507–0033, Japan
[2]Toyohashi University of Technology, 1–1 Hibarigaoka, Tempaku-cho, Toyohashi, Aichi 441–8580, Japan
[3]Hokkaido University, Kita 8, Nishi 5, Kita-ku, Sapporo 060–0808, Japan
[4]National Institute for Materials Science, 1–2–1 Sengen, Tsukuba, Ibaraki 305–0047, Japan

The surface modification of lithium phosphate on lithium alumina titanium phosphate (LATP) by a wet chemical method densified the LATP to over 90 % at a sintering temperature of 800 °C. This temperature was approximately 300 °C lower than that of LATP without additives. Densification of LATP with lithium phosphate significantly progressed from 700 to 800 °C, and endothermic peaks corresponding to its melting were found in a similar temperature range, suggesting that the densification mechanism would be due to liquid phase sintering. The liquid phase of Li_3PO_4 is produced by a multi-step thermal decomposition involving the reaction with LATP. The sintered LATP with lithium phosphate showed a density of about 90 % and the highest ionic conductivity of 3.5×10^{-4} S/cm at 25 °C, suggesting an excellent Li ion conducting, solid electrolyte material.

Key-words : LATP, Li_3PO_4, Surface modification, Low-temperature sintering, In-situ SEM

[Received December 29, 2023; Accepted March 6, 2024]

1. Introduction

All-solid-state lithium-ion batteries (ASSLiBs) consist of solid materials for all components including the electrolyte and electrode active materials.[1)–4)] ASSLiBs with oxide-based electrolytes are expected to be the next-generation batteries. Compared to conventional batteries with liquid electrolytes, they are superior in safety and durability. They are expected to be applied in a wide range of fields, such as IoT, mobility, and energy storage systems (microgrids), as the next-generation rechargeable battery.[5)–8)] Besides oxides, polymer, halide and sulfide materials are used as ASSLiB electrolytes. Among these materials, oxide materials lack plasticity and require a sintering process in addition to the powder pressurization process for the densification and junction of the cell components. This process can join the particles and component interfaces, and good Li-ion conduction pathways are formed. The one-step co-sintering process is one of the efficient methods for sintering battery green cells.[9)–12)] The sequential co-sintering method, in which the deposition and sintering of each component are repeated, requires multiple sintering cycles. The one-step co-sintering method, in which sequential deposition followed by sintering of all the components is performed at once, is a more efficient way. The one-step co-sintering temperature is limited to the lowest melting point of the component materials. In general, the active material often has a lower sintering temperature than the electrolyte material, so the co-sintering temperature is limited to the sintering temperature of the electrode.[13)–15)] The electrolyte material must be densely sintered together with the electrode in a restricted temperature range, and the interfaces between different phases, such as the electrolyte/electrode layer interface within the composite electrode, must be well-bonded. For this reason, low-temperature sintering methods have been developed that can sufficiently densify the electrolyte at lower temperatures.

Various methods have been used for the low-temperature sintering of electrolytes, including element substitution,[16)–20)] minimization of particle size by ball-milling and liquid-phase synthesis,[19),21)–25)] the addition of sintering aids,[26)–31)] and sintering techniques such as hot pressing, spark plasma sintering, and cold sintering.[20),32)–37)] For the method of adding a sintering additive, the additive melts at a lower temperature than the base material. It fills the gaps between the particles of the base material, thereby densifying the material. When this process is applied to electrolyte materials, the microstructure must be densified, and good Li-ion conduction pathways must be formed without forming highly resistive phases. Therefore, there is a need to select sintering additives that do not significantly impair the characteristics of the base material and a method that allows for the uniform addition of a minimum

† Corresponding author: K. Ishii; E-mail: ishii.kento@nitech.ac.jp
‡ Corresponding author: T. Uchikoshi; E-mail: UCHIKOSHI.Tetsuo@nims.go.jp

amount of additives. In the field of batteries, surface modification methods for improving the electrochemical stability of electrode active materials have been well studied. These methods are expected to be applied as surface modification methods for electrolyte materials.[38)–48)]

Among the oxide-based solid electrolytes, the NASICON-type $Li_{1.3}Al_{0.3}Ti_{1.7}(PO_4)_3$ (LATP) has excellent properties; i.e., high lithium-ion conductivity, low cost, low toxicity, and easy synthesis.[19),20),23),49),50)] In addition, it has an excellent chemical stability in air and water.[51)–54)] In the past, cathode active materials compatible with LATP electrolytes have been investigated.[13),14),55)–59)] Considering the thermal stability of the active materials and their reactivity with LATP, the co-sintering process should be performed at a temperature of 800 °C or below. However, since the sintering temperature required for LATP is around 950 °C, it is necessary to lower the temperature. It has been reported that trace amounts of Co elements in Co-based cathode active materials diffuse into the LATP phase, thereby densifying the LATP phase.[56),59)–62)] These studies suggested that lithium phosphate salts, which are formed as intermediate products during the reaction of Co with LATP, improve the sinterability of LATP. Various lithium salts, such as $LiBO_2$, Li_3BO_3, Li_2CO_3, LiCl, LiOH and Li_3PO_4, have been applied as sintering additives for LATP.[27)–29),31),63)–65)] Lithium phosphate is a known lithium ion conductor and is expected to be a sintering aid that does not block the Li-ion conduction of LATP at its grain boundaries.[66)–70)] It has been reported that LATP with Li_3PO_4 is densified at a sintering temperature of 800 °C, which is lower than the melting point of Li_3PO_4, 837 °C, but the sintering mechanism has not been revealed. The sintering at temperatures lower than the melting point of the sintering aid may be due to the contribution of an intermediate phase produced by the reaction between the matrix phase and the aid. The actual melting occurs at temperatures lower than the melting point in many material systems has been reported, but the mechanism is still not clarified.[71),72)] In this study, the effectiveness of the wet chemical method for the uniform addition of the Li_3PO_4 sintering aid to LATP is investigated, and the effects on the sintering mechanism and electrical conductivity are discussed.

2. Experimental procedure

2.1 Sample preparation

Figure 1 shows the preparation process of the Li_3PO_4-modified LATP (LATP-Li_3PO_4) powder and particles. Commercially-available LATP powder (Toshima Manufacturing Co., Ltd., Japan) having the average particle size (D_{50}) of 0.6 µm with the NASICON structure and *R*-3*c* space group, lithium acetate dihydrate ($CH_3COOLi{\cdot}2H_2O$, Nacalai Tesque, Inc., Japan), phosphoric acid (H_3PO_4, 85 wt % concentration, Kanto Chemical Co., Inc., Japan), and reagent-grade ethanol (C_2H_5OH, 99.5 % concentration, Nacalai Tesque, Inc., Japan) were used for the experiments. The impurity elements and their amounts contained in the LATP powder are shown in Table S1. Lithium acetate dihydrate was dissolved in the ethanol solvent so that the amount of the Li content in Li_3PO_4 relative to LATP was $x = 0.0$, 0.1, 0.2, 0.3, 0.5, 1.0, 2.0 wt %. While the solution was being ultrasonicated, 15-vol % LATP powder was dispersed in this solution. H_3PO_4 was then added to the slurry while stirring. Lithium acetate dihydrate and phosphoric acid were added in the molar ratio of 3:1. Li_3PO_4 was precipitated on the LATP particle surface by the reaction of lithium acetate and phosphoric acid, as expressed by Eq. (1).[73)]

$$3CH_3COOLi{\cdot}2H_2O + H_3PO_4 \rightarrow Li_3PO_4 \downarrow + 3CH_3COOH + 2H_2O \quad (1)$$

The prepared slurry was dried at 100 °C for 1 h using a hot plate, and the LATP-Li_3PO_4 powder was obtained. The coarse agglomerates of the dried powder were crushed with an agate mortar, then the powder was thermally treated at 400 °C for 1 h in air at the heating rate of 200 °C/h to remove the produced acetic acid. The powder was uniaxially pressed into a disk shape with a 10-mm diameter and 1-mm thickness at 100 MPa. The green bodies were fired at 800 °C for 10 h in air at the heating rate of 200 °C/h.

2.2 Sample characterization

The relative densities of the LATP-Li_3PO_4 fired bodies were calculated by measuring the bulk density of the Li_3PO_4-LATP. The thickness at five locations and the diameter at four locations were measured with respect to the disk-shaped samples, and the volume was calculated from the average of these measurements. The bulk density of the samples was calculated from the measured weight and volume. The presence of any reaction phases was evaluated by a powder X-ray diffraction (XRD) measurement (RINT-TTRIII, Rigaku Corp., Japan). The state of the Li_3PO_4 modification on the surface of the LATP particles was evaluated by Fourier-transform infrared spectroscopy and the attenuated total reflection method (ATR-FTIR) (IRSprit with QATR-S, Shimadzu Corp., Japan). The differential scanning calorimetry (DSC) of LATP-Li_3PO_4 was measured from 25 to 1050 °C in air at the heating rate of 10 °C/min using a thermal analyzer (DSC3300SA, Bruker AXS, Inc., MA, USA). The frac-

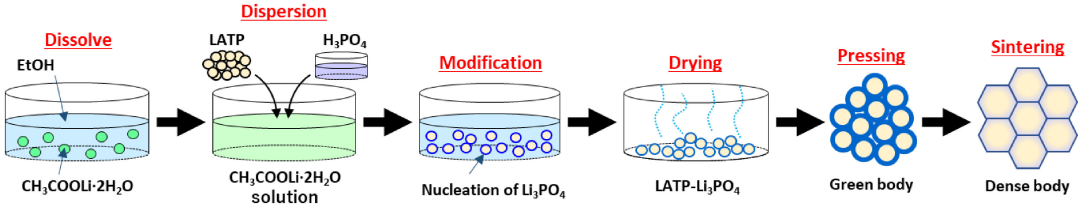

Fig. 1. The preparation process of the LATP-Li_3PO_4.

tured surface (FS) of the LATP-Li_3PO_4 fired bodies was observed by a scanning electron microscope (SEM) (JSM-6500F, JEOL Ltd., Japan). The FS of the fired specimens was etched by an argon-ion milling cross-section polisher (IB-09020CP, JEOL Ltd., Japan), and the microstructure observations and elemental analysis were performed by SEM-EDS (JSM-7800F, JEOL Ltd., Japan). The morphology change in the LATP-Li_3PO_4 powder during heating was characterized by an in-situ SEM (JSM-IT200 with an attached heating stage, JEOL Ltd., Japan). All the fired disc-shaped LATP-Li_3PO_4 pellets were polished and coated with Au electrodes on both sides using a sputtering apparatus (SC-701, Sanyu Electronics Co., Ltd., Japan). The Au-coated samples were sealed in a glass container filled with Argon gas to avoid the sub-reaction during the electrochemical testing. The electrical conductivity was measured using an impedance analyzer (VSP-300, Bio-Logic Science Instruments, Ltd., France) in the frequency range from 7 MHz to 0.1 Hz with the AC amplitude of 14 mV at temperatures from 25 to 125 °C.

3. Results and discussion

3.1 Powder characteristics

The liquid-phase synthesis based on the Eq. (1) reaction lead to the synthesis of the highly-crystalline single-phase Li_3PO_4, as shown in Fig. S1. The peaks of the Li_3PO_4 phase could not be detected from the XRD pattern of LATP modified with Li_3PO_4 because the amount of Li_3PO_4 modification is minimal. Instead, the peaks of the LATP powder modified with Li_3PO_4 were very similar to those of the unmodified LATP powder, indicating that no decomposition or side reactions of the LATP phase occurred during the liquid-phase treatment. EDS mapping of the Li_3PO_4 modified LATP powder showed the presence of a large amount of the P element, suggesting the presence of phosphorus compounds (probably Li_3PO_4) on the surface of the treated powder, as shown in Fig. S2. We also attempted to characterize the surface of the treated powders by transmission electron microscopy, but the results did not directly indicate the presence of the Li_3PO_4 phase, because Li_3PO_4 is susceptible to electron beam damage. The ATR-FTIR spectrum of the LATP-Li_3PO_4 powders ($x = 0.0$–2.0) thermally treated at 400 °C and Li_3PO_4 powder is shown in Fig. S3. The peaks around 1000 cm^{-1} are attributed to the asymmetric and symmetric stretching vibrations of the P–O bond in the PO_4^{3-} tetrahedral.[74)–76)] The absorption peak intensity at 1018 cm^{-1} increased with the increase in the addition amount x. The peaks below 750 cm^{-1} are due to the Ti–O stretching vibrations in the TiO_6 hexahedron and asymmetric modulation vibrations of the O–P–O bonds in the PO_4^{3-} tetrahedron. The peak at 1455 cm^{-1} is due to vibrations of the Al–O bond. With the increasing Li_3PO_4 addition, the peak intensities originating from the vibrations of the Al–O and Ti–O bonds decreased and the spectrum gradually approached that of Li_3PO_4.[77)–79)] These results suggest that Li_3PO_4 is modified on the surface of LATP.

3.2 Relative density

Figure 2 shows the relative densities of LATP-Li_3PO_4 ($x = 0.0$–2.0) sintered at 600, 700, and 800 °C and its compact. The LATP-Li_3PO_4 sintered at 600 °C was not densified at any addition amount of $x = 0.0$–2.0, and its density was similar to that of the green body. Densification of Li_3PO_4-unmodified LATP ($x = 0.0$) had not significantly progressed at any sintering temperature between 600–800 °C. On the other hand, LATP-Li_3PO_4 ($x = 0.1$–2.0) densified with the increasing sintering temperature from 600 to 800 °C. At the sintering temperature of 800 °C, the sintered density was 63 % at $x = 0.0$ and the sintered density was about 90 % at $x = 0.1$–2.0. Since LATP sintered at 1100 °C showed a density of about 90 %, the sintering temperature of LATP could be lowered by 300 °C with the addition of Li_3PO_4. **Figure 3** shows the relative densities of LATP, Li_3PO_4 and LATP-Li_3PO_4 ($x = 0.3$) versus the sintering temperature. The single LATP exhibited a maximum sintering density at 1100 °C. The density of Li_3PO_4 rapidly increased between 600 and 800 °C, with a maximum sintered density of 87 % at 800 °C, followed by a decrease in the sintered density toward 900 °C. The decrease in the density of Li_3PO_4 from 800 to 900 °C is due to the phase transition from the solid to liquid phase as the melting proceeded. The decrease in density above 900 °C is probably due to the formation of shrinkage cavities during

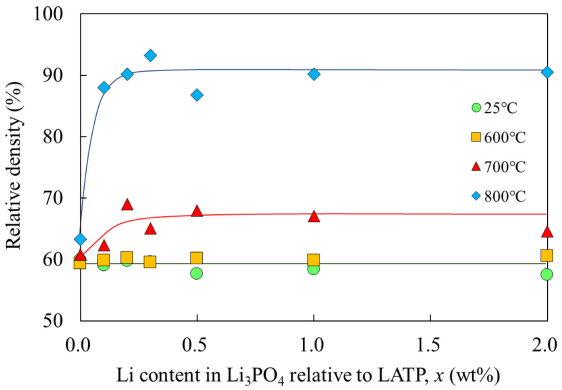

Fig. 2. Relative densities of LATP-Li_3PO_4 fired at temperatures of 600, 700 and 800 °C, and unfired LATP-Li_3PO_4.

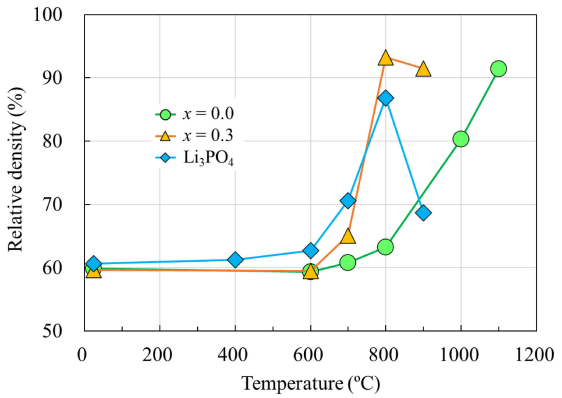

Fig. 3. The relative densities of the fired LATP-Li_3PO_4 for $x = 0.0$ and 0.3 of the Li content in Li_3PO_4 relative to LATP, and the densities of the fired Li_3PO_4.

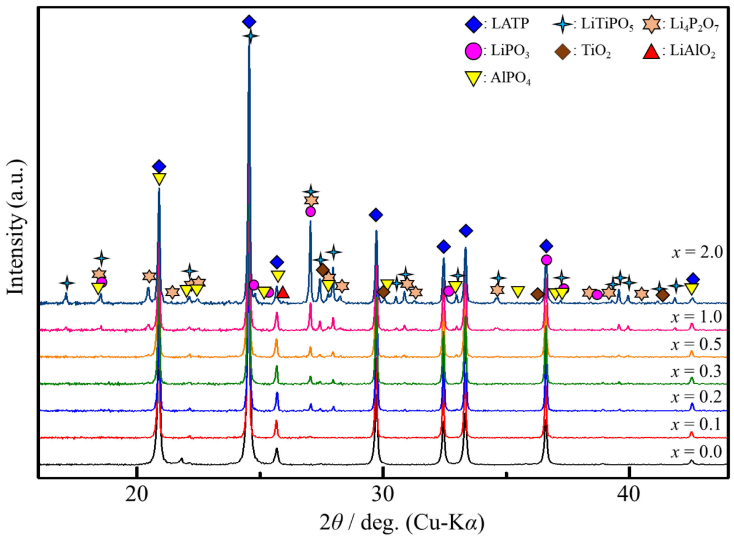

Fig. 4. The XRD patterns of the LATP-Li_3PO_4 for $x = 0.0$–2.0 of the Li content in Li_3PO_4 relative to LATP, sintered at 800 °C.

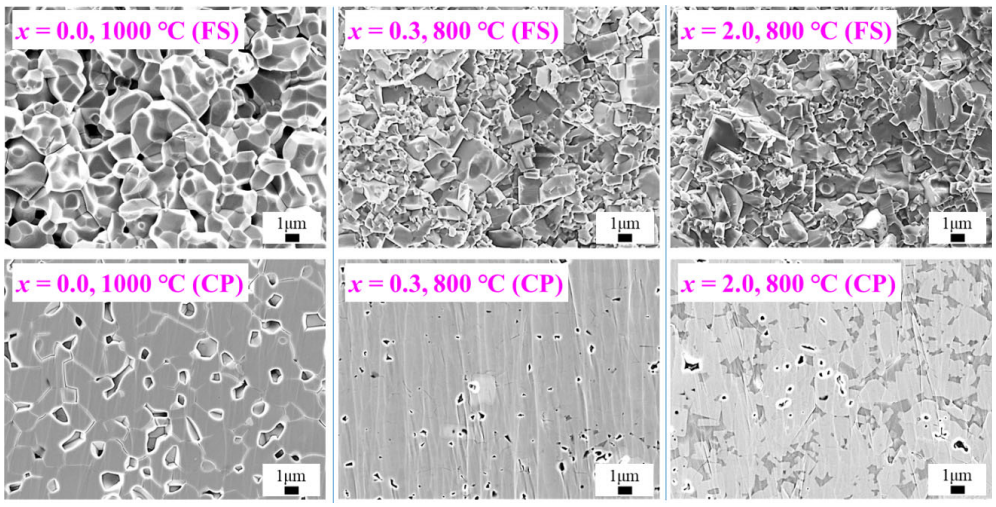

Fig. 5. The FS and the cross-section polished by Ar-ion milling (CP) of the sintered LATP-Li_3PO_4 (Li content in Li_3PO_4 relative to LATP, $x = 0.0$, 0.3 and 2.0).

the dissolution and resolidification of Li_3PO_4. In addition, the rapid melting or over-sintering may have contributed to the expansion of the residual isolated pores in the sample.[80)–83)] The sintering behavior of LATP-Li_3PO_4 ($x = 0.3$) was more similar to that of Li_3PO_4 than that of the base material, LATP. Despite the very small amount of added Li_3PO_4, the sinterability of the LATP-Li_3PO_4 system would be dominated by Li_3PO_4 and its intermediate products.

3.3 Reactivity during sintering

Figure 4 shows the XRD patterns of LATP-Li_3PO_4 ($x = 0.0$–2.0) sintered at 800 °C. As shown in the XRD measurement results in Fig. 4, no secondary phase appeared in LATP fired at 800 °C. Although not shown here, no secondary phase appeared even in the single Li_3PO_4 fired at 800 °C. On the other hand, in LATP-Li_3PO_4 fired at 800 °C, new products were clearly formed as shown in Fig. 4, and their intensity became more pronounced as the amount of Li_3PO_4 modification increased. The above suggests that when LATP and Li_3PO_4 coexist, some reaction and/or decomposition occur during firing at 800 °C. The formation of $Li_4P_2O_7$ and $LiPO_3$ by thermal decomposition of Li_3PO_4 during firing likely follows Eqs. (2)–(4). Besides Li_3PO_4 as an additive, lithium phosphates would be produced as decomposition products from the LATP phase. This is because the XRD of LATP-Li_3PO_4 before sintering did not identify the Li_3PO_4 phase, whereas the peak intensity of the lithium phosphate phase in the XRD pattern after sintering was high.

$$2Li_3PO_4 \rightarrow Li_4P_2O_7 + Li_2O \quad (2)$$

$$Li_4P_2O_7 \rightarrow 2LiPO_3 + Li_2O \quad (3)$$

$$Li_3PO_4 \rightarrow LiPO_3 + Li_2O \quad (4)$$

3.4 Microstructures and elemental mapping

Figure 5 shows that the FS and cross-section polishing (CP) microstructures of the sintered LATP-Li_3PO_4 ($x = 0.0$, 0.3 and 2.0 wt%). LATP-Li_3PO_4 ($x = 0.3$, 2.0) sin-

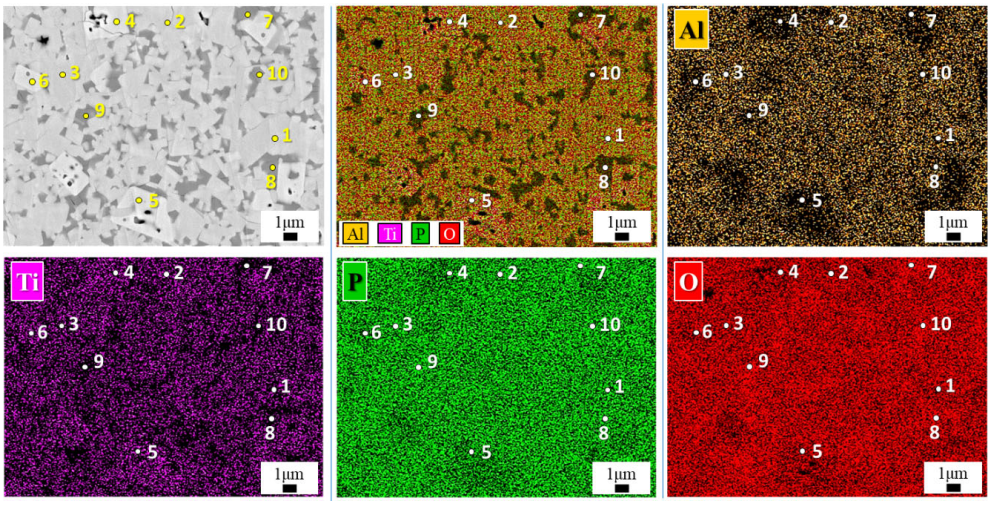

Fig. 6. The elemental mapping images of the LATP-Li_3PO_4 (Li content in Li_3PO_4 relative to LATP, $x = 2.0$) fired at 800 °C.

Table 1. The elemental ratios at each point in the EDS analysis

Spectrum/At%	Al	Ti	P	O	O/P	Condition	Predicted Phase
Spot 1	2.7	8.6	17.0	71.7	4.2	Al-rich	LATP
Spot 2	2.6	7.8	15.7	73.6	4.7	Al-rich	LATP
Spot 3	2.3	9.1	17.0	71.6	4.2	Al-rich	LATP
Spot 4	—	12.8	14.3	72.8	5.1	No Al content	$LiTiPO_5$
Spot 5	—	12.2	14.7	73.1	5.0	No Al content	$LiTiPO_5$
Spot 6	—	12.8	13.5	73.7	5.5	No Al content	$LiTiPO_5$
Spot 7	0.8	4.8	20.0	74.3	3.7	Al, Ti-poor	Li_3PO_4, $Li_4P_2O_7$
Spot 8	1.3	5.2	19.1	74.5	3.9	Ti-poor	LATP, Li_3PO_4
Spot 9	0.6	2.1	27.8	69.4	2.5	Al- and Ti-poor, P-rich	$LiPO_3$, P_2O_5
Spot 10	1.7	5.4	22.6	70.3	3.1	Ti-poor, P-rich	$Li_4P_2O_7$, $LiPO_3$
Whole region	1.9	8.6	18.2	71.4	3.9	—	Li_3PO_4-LATP ($x = 2.0$)
LATP (Theoretical)	1.8	10.2	18	72	4.0	Amount of 6 molar LATP	—

tered at 800 °C formed a denser microstructure than LATP sintered at 1000 °C. The LATP sintered at 1100 °C was dense but very brittle due to intergranular cracking in its structure as shown in Fig. S4. The densities of the sintered LATP-Li_3PO_4 were calculated by the dimension measurement and image analysis as shown in Table S2. The calculated density of the LATP single-phase by the image analysis was similar to that obtained from the dimension measurements. However, the calculated densities of LATP-Li_3PO_4 ($x = 0.3$ and 2.0) by the image analysis were higher than those obtained from the dimension measurements. The SEM image of the fracture surface was taken at the center of the sample, and the SEM image of the polished surface was taken relatively close to the sample surface. Therefore, it is conceivable that the denseness of the sample surface and the sparseness of the interior affected the results of the two analytical methods. Furthermore, the reaction products may have caused errors in the calculation of the theoretical density of LATP-Li_3PO_4. In the case of LATP-Li_3PO_4, no intergranular cracks were formed, and the addition of Li_3PO_4 was also effective in densifying LATP without intergranular cracks. The LATP-Li_3PO_4 sintered at 800 °C had a relative density of 93 % and the same density as the single LATP sintered at 1100 °C which had a relative density of 91 %, but its grain growth had not progressed. This suggested that the melting of the added Li_3PO_4 densified the microstructure. In the CP image of LATP-Li_3PO_4 at $x = 2.0$, some segregates with a dark contrast were present in the microstructure, but no segregated phases were found in the microstructure at $x = 0.3$. At $x = 2.0$, the amount of the Li_3PO_4 addition was excessive, and Li_3PO_4 was segregated to the grain boundaries. When the amount of Li_3PO_4 added is $x = 0.3$, Li_3PO_4 as a sintering aid, does not segregate at the LATP grain boundaries. In addition, an elemental analysis was performed to characterize the segregated phases of the LATP-Li_3PO_4.

Figure 6 and **Table 1** show the EDX elemental mapping and point spectrum of LATP-Li_3PO_4 ($x = 2.0$) sintered at 800 °C, respectively. From the mapping images, three main phases were identified, i.e., the LATP matrix phase (spots 1, 2, and 3), the Al-poor phase with a lighter contrast (spots 4, 5, and 6), and the Ti-poor phase with a darker contrast (spots 7, 8, 9, and 10). The ratio of the elements present in the entire image area was similar to the theoretical value of LATP as shown in Table 1. The phases in spots 1, 2, and 3 can be regarded as the LATP phases, although they are somewhat enriched in Al elements. The phases in spots 4, 5 and 6 are presumed to be the $LiTiPO_5$

phases since they contain no Al and have an O/P ratio = 5. Spots 7, 8, 9, and 10 are Ti-poor phases, and their O/P ratios suggested that they are ortho-, pyro-, and meta-lithium phosphate salts.

3.5 Thermal analysis

Figure 7 shows the DSC curves of LATP-Li_3PO_4 at $x = 0.0$ and 2.0 and Li_3PO_4. No noticeable change was observed between 600–800 °C for the single LATP. For LATP-Li_3PO_4 at $x = 0.2$, an endothermic reaction occurred between 771 and 900 °C, along with a large endothermic peak at 816 °C. In addition to this large peak, two small peaks were seen between 771–816 °C. These peaks indicated the decomposition and melting of Li_3PO_4, reaction of LATP with Li_3PO_4, and the decomposition reaction of Li_3PO_4 as shown by Eqs. (2)–(4). The reactions of Eqs. (2) and (3) sequentially proceeded at about 816 °C, so that these reactions are summarized by Eq. (4).

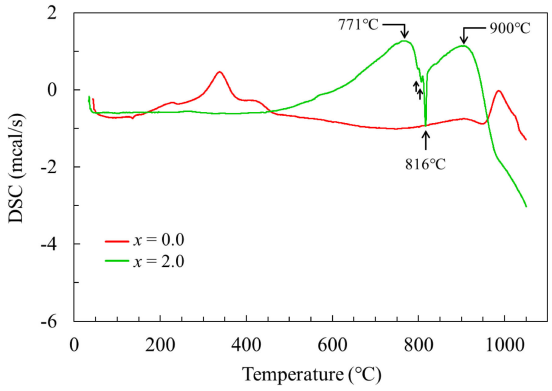

Fig. 7. The DSC curves of the LATP-Li_3PO_4 powder (Li content in Li_3PO_4 relative to LATP, $x = 0.0$ and 2.0) at the heating rate of 10 °C/min in air.

Li_3PO_4 becomes the intermediate product, $Li_4P_2O_7$, and the final product, $LiPO_3$. The melting point of Li_3PO_4 is 837 °C, and its sintering proceeded in the LATP-Li_3PO_4 system with the formation and melting of $LiPO_3$. This is because the melting point of $LiPO_3$ is 650 °C[29),70),84)] thus the produced $LiPO_3$ immediately melts at 800 °C. The melting of Li_3PO_4 is accompanied by thermal decomposition and melting of the other lithium phosphate compounds. Therefore, the melting point of the Li_3PO_4 single phase is 837 °C, but in the LATP-Li_3PO_4 system, the liquid phase is formed at a temperature lower than the melting point of Li_3PO_4, and sintering occurs. The sintering mechanism of LATP-Li_3PO_4 was suggested to be liquid phase sintering as already described.

3.6 In-situ SEM observation

Figures 8(a) and 8(b) show the morphology of the LATP and LATP-Li_3PO_4 ($x = 2.0$) secondary particles during heating as observed by in-situ SEM, respectively. Morphological changes in the secondary particles during the sintering and shrinking process were analyzed by ImageJ, an image analysis software program.[85)–87)] The

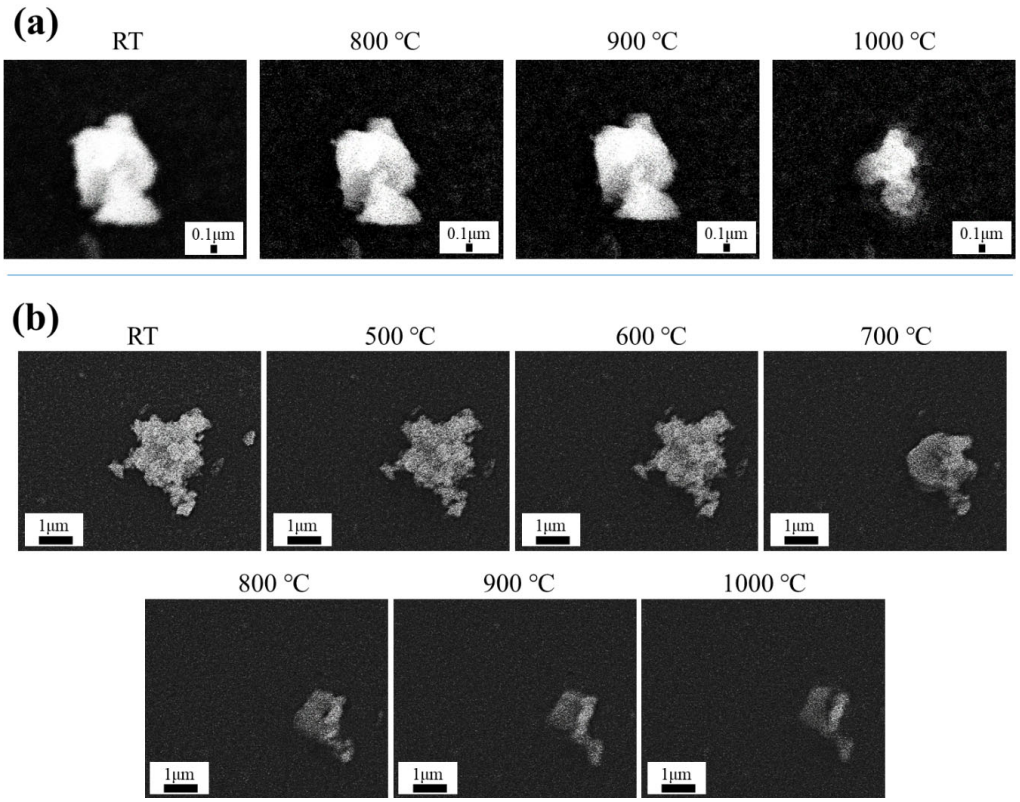

Fig. 8. (a) The morphology of the LATP particles during heating observed by in-situ SEM, (b) the morphology of the LATP-Li_3PO_4 (Li content in Li_3PO_4 relative to LATP, $x = 2.0$) particles during heating observed by in-situ SEM.

SEM images at each temperature were classified into particle and spatial areas by a binarization process, and the values of the secondary particle areas were calculated. Their area shrinkage rates were calculated as the difference between the secondary particle area at room temperature and at each temperature. The actual sample dimensions were measured before and after sintering, and the volumetric shrinkage was determined. **Figures 9**(a) and 9(b) show the sintering shrinkage rates of the LATP and LATP-Li_3PO_4 ($x = 2.0$) calculated by a sample dimensional measurement and image analysis. Although the secondary particles observed in situ were only a few microns in diameter and not composed of many primary particles, the measured and calculated shrinkage rates at each temperature were similar. Therefore, the morphological change in the particles during heating observed by in-situ SEM is considered to represent the sintering behavior in the entire bulk body. For LATP-Li_3PO_4 ($x = 2.0$), the morphology of the secondary particle changed and significantly shrank from 600 to 800 °C. During the initial stage of sintering up to 700 °C, the shrinkage progressed by −25 % of about half the total, and the primary particles joined each other into a single particle form. At this intermediate stage as shown in **Fig. 10**, it is considered that several pores remained in the integrated particle group.[80)–83)] Furthermore, during the final stage of sintering from 700 to 800 °C, the shrinkage progressed by −20 %, and the joined particles became smaller while maintaining their shape. The melting temperature range was understood to be 771–816 °C based on the DSC measurement results; the integration of the particle group seemed to occur before the melting of the lithium phosphate.

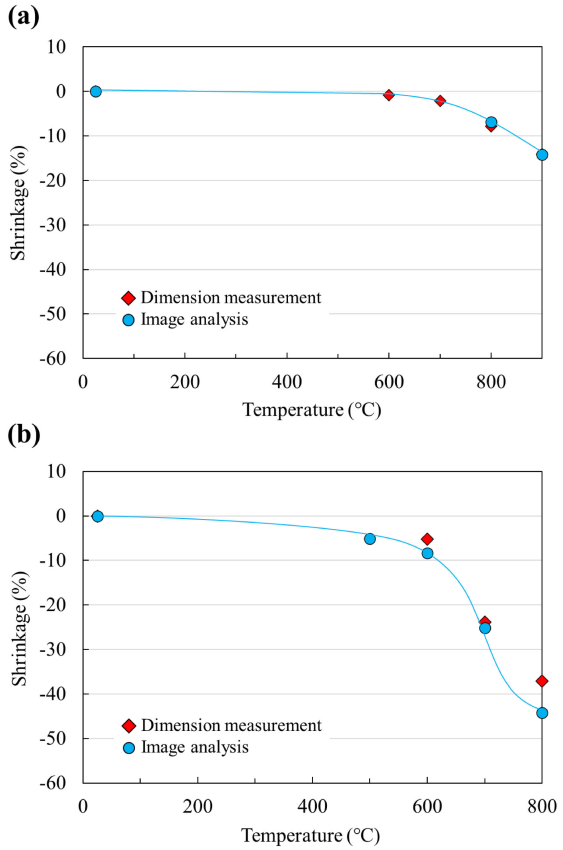

Fig. 9. The thermal shrinkages of (a) LATP and (b) LATP-Li_3PO_4 (Li content in Li_3PO_4 relative to LATP, $x = 2.0$) calculated by size measurement and in-situ SEM image analysis.

3.7 Electrical conductivity

The Nyquist plots of LATP-Li_3PO_4 ($x = 0.0$–2.0) measured by the AC impedance method exhibited a clear semicircle as shown in Fig. S5. From the origin to the x-axis intercept of the arc is the bulk resistance (R_b), the semi-circular arc is the grain boundary resistance (R_{gb}) and pseudo-capacitance (CPE1), and in the low-frequency region, the electric double layer corresponds to the pseudo-capacitance (CPE2), similar to the equivalent circuit in Fig. S5. The relaxation frequencies of LATP-Li_3PO_4 obtained from the semicircles corresponding to the grain boundary impedance are shown in Table S3. The relaxation frequencies are similar between $x = 0.1$ and 1.0, except $x = 0.0$ (pure LATP) and $x = 2.0$ (excess Li_3PO_4-added LATP), indicating that there was no significant change in the grain boundary composition.

Figure 11(a) shows the electrical conductivity of LATP-Li_3PO_4 ($x = 0.0$–2.0) calculated from the Nyquist plot. The electrical conductivity at 25 °C of LATP-Li_3PO_4 ($x = 0.0$–2.0) is shown in Fig. 11(b). The electrical conductivity of LATP-Li_3PO_4 increased from $x = 0.0$ to 0.2, then remained constant until $x = 0.5$. The electrical conductivity decreased above $x = 0.5$. From $x = 0.0$ to 0.2, the conductivity increased due to the increased sintering density

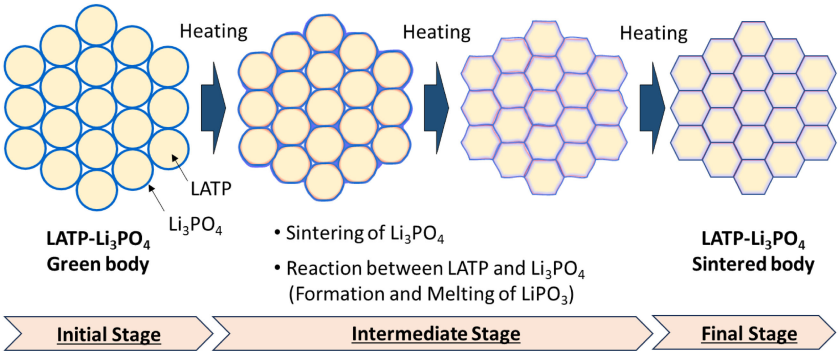

Fig. 10. The sintering mechanism of the LATP-Li_3PO_4.

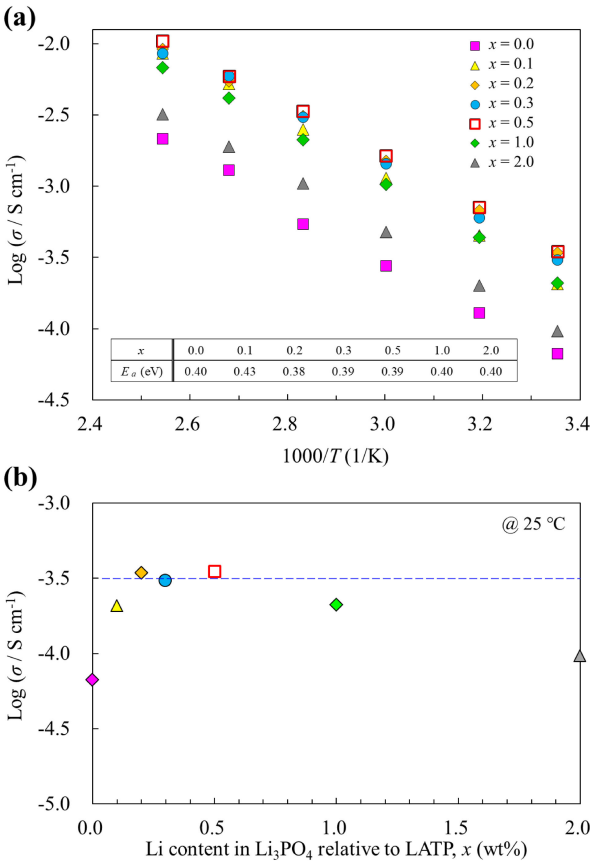

Fig. 11. (a) The electrical conductivities of the LATP-Li_3PO_4 (Li content in Li_3PO_4 relative to LATP, $x = 0.0$–2.0) body fired at 800 °C, (b) the electrical conductivity at 25 °C of the LATP-Li_3PO_4 at $x = 0.0$–2.0.

and decreased length of the lithium conduction pathways. For $x = 0.2$–0.5, the sintered density did not change and the added Li_3PO_4 was uniformly present without segregation, so there was no significant change in the conductivity. The decrease in conductivity at $x = 0.5$–2.0 is due to the excess amount of segregated Li_3PO_4 acting as a resistive phase, and the significantly increased amount of the reaction phases. No significant changes were observed in any of the activation energies. The grain boundary component accounts for a large fraction of the total conductivity, and the activation energy also depends on factors related to the grain boundary. Since the amount of Li_3PO_4 added by this modification method was minimal and the amount of the reaction phase formed between the LATP particles was very small, it is postulated that there was no change in the activation energy. LATP sintered at 800 and 1000 °C exhibited an electrical conductivity of 6.7×10^{-5} and 2.7×10^{-4} S/cm at 25 °C, respectively. LATP-Li_3PO_4 ($x = 0.5$ wt %) sintered at 800 °C exhibited the highest electrical conductivity of 3.5×10^{-4} S/cm at 25 °C. The obtained conductivities of LATP-Li_3PO_4 were comparable to or exceeded those of previous reports.[29),88)] The difference in these values is due to the addition method of the sintering aid. Sintering aids were added by the powder mixing method in previous reports and by surface modification utilizing the wet chemical reaction method in this study. The powder mixing method is simple, but its structure tends to be heterogeneous, resulting in a low conductivity. The surface modification method can uniformly add the sintering aid and form a more homogeneous microstructure without segregation resulting in a higher conductivity. By surface-modifying the electrolyte particles using a wet chemical reaction method, a minimum amount of sintering aid can be added uniformly, and as a result, a sintered body with a uniform structure can be obtained. Li_3PO_4 effectively acts as a sintering aid for LATP, and LATP with a sintered density equivalent to 1100 °C can be obtained at a sintering temperature of 800 °C. As a result, LATP-Li_3PO_4 sintered at 800 °C exhibits high electrical conductivity.

4. Conclusions

LATP-Li_3PO_4 was densified to more than 90 % relative density by sintering up to 800 °C, and its sinterability was rather higher than that of single Li_3PO_4, suggesting the interface reaction between Li_3PO_4 and LATP contributed to the improvement of sinterability of LATP-Li_3PO_4. The sintering of LATP-Li_3PO_4 was found to be not only due to the sintering and melting of Li_3PO_4, but also to a liquid phase sintering mechanism related to the melting of some lithium phosphates formed by the reaction of LATP and Li_3PO_4. Although several reaction phases were formed during the sintering of LATP-Li_3PO_4, it was possible to achieve both a high sintering density and high electrical conductivity by adding the minimum amount of Li_3PO_4 by this surface-modification method.

Acknowledgments We thank Ms. Makiko Oshida at the National Institute for Materials Science Battery Research Platform for her help with the argon-ion milling and SEM-EDS measurements. The authors wish to thank Dr. Hiroyo Segawa in the Electroceramics Group, Research Center for Functional Materials, NIMS, for her help with the DSC measurements. We thank Ms. Masae Sawamoto at Hokkaido University for her help with the in-situ SEM measurements. This study was supported in part by the Materials Processing Science Project ("Materealize"), grant number JPMXP0219207397 from MEXT, and supported by JST, PRESTO Grant Number JPMJPR21Q8, Japan.

Supporting Information Figures and photographs that could not be included in the main part of this paper can be referred to as "Supplemental materials".

References

1) K. Takada, *Acta Mater.*, **61**, 759–770 (2013).
2) S. Sen, E. Trevisanello, E. Niemöller, B. X. Shi, F. J. Simon and F. H. Richter, *J. Mater. Chem. A*, **9**, 18701–18732 (2021).
3) R. Chen, W. Qu, X. Guo, L. Li and F. Wu, *Mater. Horizons*, **3**, 487–516 (2016).
4) L. Liang, X. Sun, J. Zhang, J. Sun, L. Hou, Y. Liu and C. Yuan, *Mater. Horizons*, **6**, 871–910 (2019).
5) J. B. Goodenough and Y. Kim, *Chem. Mater.*, **22**, 587–603 (2010).

6) Y. Zhu, J. C. Gonzalez-Rosillo, M. Balaish, Z. D. Hood, K. J. Kim and J. L. M. Rupp, *Nat. Rev. Mater.*, **6**, 313–331 (2021).
7) R. Chen, Q. Li, X. Yu, L. Chen and H. Li, *Chem. Rev.*, **120**, 6820–6877 (2020).
8) X. Chen, Z. Guan, F. Chu, Z. Xue, F. Wu and Y. Yu, *InfoMat*, **4**, 1–20 (2022).
9) G. Ye, F. Ju, C. Lin, S. Gopalan, U. Pal and D. A. Seccombe, *Proc. - Electrochem. Soc.*, **PV 2005-07**, 451–459 (2005).
10) P. Xu, W. Rheinheimer, S. N. Shuvo, Z. Qi, O. Levit, H. Wang, Y. Ein-Eli and L. A. Stanciu, *ChemElectroChem*, **6**, 4576–4585 (2019).
11) B. Wang, L. Bi and X. S. Zhao, *J. Eur. Ceram. Soc.*, **38**, 5620–5624 (2018).
12) C. Seok, J. Moon, M. Park, J. Hong, H. Kim, J. W. Son, J. H. Lee, B. K. Kim, H. W. Lee and K. J. Yoon, *J. Eur. Ceram. Soc.*, **36**, 1417–1425 (2016).
13) Y. Wu, S. Wang, H. Li, L. Chen and F. Wu, *InfoMat*, **3**, 827–853 (2021).
14) L. Miara, A. Windmüller, C. L. Tsai, W. D. Richards, Q. Ma, S. Uhlenbruck, O. Guillon and G. Ceder, *ACS Appl. Mater. Inter.*, **8**, 26842–26850 (2016).
15) K. J. Kim and J. L. M. Rupp, *Energ. Environ. Sci.*, **13**, 4930–4945 (2020).
16) S. Ramakumar, C. Deviannapoorani, L. Dhivya, L. S. Shankar and R. Murugan, *Prog. Mater. Sci.*, **88**, 325–411 (2017).
17) M. M. Raju, F. Altayran, M. Johnson, D. Wang and Q. Zhang, *Electrochem*, **2**, 390–414 (2021).
18) A. Rossbach, F. Tietz and S. Grieshammer, *J. Power Sources*, **391**, 1–9 (2018).
19) J. A. Dias, S. H. Santagneli and Y. Messaddeq, *J. Phys. Chem. C*, **124**, 26518–26539 (2020).
20) K. Yang, L. Chen, J. Ma, Y. He and F. Kang, *InfoMat*, **3**, 1195–1217 (2021).
21) L. Xingang, T. Jiang, J. Fu, R. Yuan, H. Wen and C. Zhang, *ACS Appl. Mater. Inter.*, **9**, 11696–11703 (2017).
22) Y. Ren, H. Deng, H. Zhao, Z. Zhou and Z. Wei, *Ionics*, **7**, 6049–6056 (2020).
23) R. Dewees and H. Wang, *ChemSusChem*, **12**, 3713–3725 (2019).
24) K. Waetzig, A. Rost, C. Heubner, M. Coeler, K. Nikolowski, M. Wolter and J. Schilm, *J. Alloy. Compd.*, **818**, 153237 (2020).
25) L. Vijayan and G. Govindaraj, *J. Phys. Chem. Solids*, **72**, 613–619 (2011).
26) X. Zhang, T. S. Oh and J. W. Fergus, *J. Electrochem. Soc.*, **166**, A3753–A3759 (2019).
27) H. Aono, E. Sugimoto, Y. Sadaoka, N. Imanaka and G. ya Adachi, *Chem. Lett.*, **19**, 331–334 (1990).
28) H. Aono, E. Sugimoto, Y. Sadaoka, N. Imanaka and G. ya Adachi, *Solid State Ionics*, **47**, 257–264 (1991).
29) K. Waetzig, C. Heubner and M. Kusnezoff, *Crystals*, **10**, 408 (2020).
30) S. Chen, X. Hu, W. Bao, Z. Wang, Q. Yang, L. Nie, X. Zhang, J. Zhang, Y. Jiang, Y. Han, C. Wan, J. Xie, Y. Yu and W. Liu, *Cell Reports Phys. Sci.*, **2**, 0–16 (2021).
31) H. Bai, J. Hu, X. Li, Y. Duan, F. Shao, T. Kozawa, M. Naito and J. Zhang, *Ceram. Int.*, **44**, 6558–6563 (2018).
32) P. M. G. Puente, S. Song, S. Cao, L. Ziwen, X. Xiang, Q. Shen and F. Chen, *J. Adv. Ceram.*, **10**, 933–972 (2021).
33) N. Hamao, Y. Yamaguchi and K. Hamamoto, *Materials*, **14**, 4737 (2021).
34) Y. Liu, Q. Sun, D. Wang, K. Adair, J. Liang and X. Sun, *J. Power Sources*, **393**, 193–203 (2018).
35) H. Zhu, A. Prasad, S. Doja, L. Bichler and J. Liu, *Nanomaterials-Basel*, **9**, 6–8 (2019).
36) Y. Liu, J. Liu, Q. Sun, D. Wang, K. R. Adair, J. Liang, C. Zhang, L. Zhang, S. Lu, H. Huang, X. Song and X. Sun, *ACS Appl. Mater. Inter.*, **11**, 27890–27896 (2019).
37) A. Paolella, W. Zhu, G. Bertoni, A. Perea, H. Demers, S. Savoie, G. Girard, N. Delaporte, A. Guerfi, M. Rumpel, H. Lorrmann, G. P. Demopoulos and K. Zaghib, *Adv. Mater. Interfaces*, **7**, 2000164 (2020).
38) J. M. Kim, X. Zhang, J. G. Zhang, A. Manthiram, Y. S. Meng and W. Xu, *Mater. Today*, **46**, 155–182 (2021).
39) H. Zhang, J. Xu and J. Zhang, *Front. Mater.*, **6**, 1–10 (2019).
40) Z. Chen, Y. Qin, K. Amine and Y. K. Sun, *J. Mater. Chem.*, **20**, 7606–7612 (2010).
41) X. Bian, Q. Fu, X. Bie, P. Yang, H. Qiu, Q. Pang, G. Chen, F. Du and Y. Wei, *Electrochim. Acta*, **174**, 875–884 (2015).
42) H. Chen, L. Xiao, H. Chen, Y. Zhu, K. Xiang and H. Liao, *Electrochim. Acta*, **344**, 1–11 (2020).
43) Z. Chen, D. Chao, J. Lin and Z. Shen, *Mater. Res. Bull.*, **96**, 491–502 (2017).
44) V. Mereacre, N. Bohn, P. Stüble, L. Pfaffmann and J. R. Binder, *ACS Appl. Energ. Mater.*, **4**, 4271–4276 (2021).
45) W. Guo, Y. Meng, Y. Hu, X. Wu, Z. Ju and Q. Zhuang, *Front. Energy Res.*, **8**, 1–20 (2020).
46) C. Li, H. P. Zhang, L. J. Fu, H. Liu, Y. P. Wu, E. Rahm, R. Holze and H. Q. Wu, *Electrochim. Acta*, **51**, 3872–3883 (2006).
47) C. Gong, Z. Xue, S. Wen, Y. Ye and X. Xie, *J. Power Sources*, **318**, 93–112 (2016).
48) A. Banerjee, X. Wang, C. Fang, E. A. Wu and Y. S. Meng, *Chem. Rev.*, **120**, 6878–6933 (2020).
49) X. Lu, R. Wang, F. Zhang and J. Li, *Solid State Ionics*, **354**, 115417 (2020).
50) H. Aono, E. Sugimoto, N. Imanaka and G. Adachi, *J. Electrochem. Soc.*, **137**, 1023–1027 (1990).
51) K. He, C. Zu, Y. Wang, B. Han, X. Yin, H. Zhao, Y. Liu and J. Chen, *Solid State Ionics*, **254**, 78–81 (2014).
52) S. Hasegawa, N. Imanishi, T. Zhang, J. Xie, A. Hirano, Y. Takeda and O. Yamamoto, *J. Power Sources*, **189**, 371–377 (2009).
53) M. A. Pogosova, I. V. Krasnikova, A. O. Sanin, S. A. Lipovskikh, A. A. Eliseev, A. V. Sergeev and K. J. Stevenson, *Chem. Mater.*, **32**, 3723–3732 (2020).
54) E. Dashjav, Q. Ma, Q. Xu, C. L. Tsai, M. Giarola, G. Mariotto and F. Tietz, *Solid State Ionics*, **321**, 83–90 (2018).
55) M. Rumpel, F. Nagler, L. Appold, W. Stracke, A. Flegler, O. Clemens and G. Sextl, *Mater. Adv.*, **3**, 4015–4025 (2022).
56) P. Hofmann, F. Walther, M. Rohnke, J. Sann, W. G. Zeier and J. Janek, *Solid State Ionics*, **342**, 1–10 (2019).
57) M. Gellert, E. Dashjav, D. Grüner, Q. Ma and F. Tietz, *Ionics*, **24**, 1001–1006 (2018).
58) C. Y. Yu, J. Choi, V. Anandan and J. H. Kim, *J. Phys. Chem. C*, **124**, 14963–14971 (2020).
59) K. Nagata and T. Nanno, *J. Power Sources*, **174**, 832–837 (2007).

60) K. Ishii, M. Ode, K. Mitsuishi, S. Miyoshi, T. Ohno, K. Takada and T. Uchikoshi, *J. Power Sources*, 546, 231954 (2022).
61) K. Ishii, T. Uchikoshi, S. Miyoshi, M. Ode, T. Ohno and K. Takada, *Mater. Lett.*, 324, 132736 (2022).
62) K. Ishii, T. Uchikoshi and K. Takada, *J. Ceram. Soc. Jpn.*, 131, 298–305 (2023).
63) K. Kwatek, W. Ślubowska, C. Ruiz, I. Sobrados, J. Sanz, J. E. Garbarczyk and J. L. Nowiński, *J. Alloy. Compd.*, 838, 1–13 (2020).
64) B. Davaasuren and F. Tietz, *Solid State Ionics*, 338, 144–152 (2019).
65) Z. Zou, Y. Li, Z. Lu, D. Wang, Y. Cui, B. Guo, Y. Li, X. Liang, J. Feng, H. Li, C. W. Nan, M. Armand, L. Chen, K. Xu and S. Shi, *Chem. Rev.*, 120, 4169–4221 (2020).
66) E. Kartini, V. Yapriadi, H. Jodi, M. Manawan, C. Panghegar and Wahyudianingsih, *Prog. Nat. Sci.-Mater.*, 30, 168–173 (2020).
67) N. I. P. Ayu, E. Kartini, L. D. Prayogi, M. Faisal and Supardi, *Ionics*, 22, 1051–1057 (2016).
68) K. Gaur, A. J. Pathak and H. B. Lal, *J. Mater. Sci.*, 23, 4257–4262 (1988).
69) J. Li and W. Lai, *Solid State Ionics*, 351, 115329 (2020).
70) A. Robertson, J. G. Fletcher, J. M. S. Skakle and A. R. West, *J. Solid State Chem.*, 109, 53–59 (1994).
71) A. Wustrow, G. Huang, M. J. McDermott, D. O'Nolan, C. H. Liu, G. T. Tran, B. C. McBride, S. S. Dwaraknath, K. W. Chapman, S. J. L. Billinge, K. A. Persson, K. Thornton and J. R. Neilson, *Chem. Mater.*, 33, 3692–3701 (2021).
72) A. Miura, C. J. Bartel, Y. Goto, Y. Mizuguchi, C. Moriyoshi, Y. Kuroiwa, Y. Wang, T. Yaguchi, M. Shirai, M. Nagao, N. C. Rosero-Navarro, K. Tadanaga, G. Ceder and W. Sun, *Adv. Mater.*, 33, 2100312 (2021).
73) M. Hofmann, F. Nagler, M. Kapuschinski, U. Guntow and G. A. Giffin, *ChemSusChem*, 13, 5962–5971 (2020).
74) J. Li, C. Liu, C. Miao, Z. Kou and W. Xiao, *Ionics*, 28, 63–72 (2022).
75) B. Yang, X. Li, H. Guo, Z. Wang and W. Xiao, *J. Alloy. Compd.*, 643, 181–185 (2015).
76) S. He, Y. Xu, B. Zhang, X. Sun, Y. Chen and Y. Jin, *Chem. Eng. J.*, 345, 483–491 (2018).
77) A. H. Ahmad, M. Z. A. Yahya, R. Puteh and A. K. Arof, *Indones. J. Phys.*, 15, 65–69 (2016).
78) S. M. Benoy, S. Singh, M. Pandey and B. Manoj, *Mater. Res. Express*, 6, 125624 (2019).
79) A. H. Ahmad and A. K. Arof, *Ionics*, 10, 200–205 (2004).
80) G. Wang, H. Zhang, C. Liu, H. Su, L. Jia, J. Li, X. Huang and G. Gan, *J. Electron. Mater.*, 47, 4672–4677 (2018).
81) B. Wang, J. Wang, A. Chang and J. Yao, *RSC Adv.*, 9, 25488–25495 (2019).
82) R. M. German, P. Suri and S. J. Park, *J. Mater. Sci.*, 44, 1–39 (2009).
83) X. Wang, Y. Li, Z. Chen, H. Zhang, H. Su, G. Wang, Y. Liao and Z. Zhong, *J. Alloy. Compd.*, 797, 566–572 (2019).
84) R. K. Osterheld, *J. Inorg. Nucl. Chem.*, 30, 3173–3175 (1968).
85) W. S. Rasband, https://imagej.nih.gov/ij/ (1997–2018).
86) C. A. Schneider, W. S. Rasband and K. W. Eliceiri, *Nat. Methods*, 9, 671–675 (2012).
87) M. D. Abràmoff, P. J. Magalhães and S. J. Ram, *Biophoton. Int.*, 11, 36–41 (2004).
88) M. Rumpel, L. Appold, J. Baber, W. Stracke, A. Flegler and G. Sextl, *Mater. Adv.*, 3, 8157–8167 (2022).